EXPLOSIVE FIELD EMITTER PROCESSING IN SUPERCONDUCTING RF CAVITIES*

J. KNOBLOCH[†] and H. PADAMSEE

*Floyd R. Newman Laboratory of Nuclear Studies,
Cornell University, Ithaca, NY 14853, USA*

Superconducting niobium radiofrequency cavities for e^+e^- accelerators presently are limited to accelerating gradients of $25\,MV/m$ – far less than their theoretical capability of $50\,MV/m$. *Field emission* presents the main impediment to higher gradients. In many cases, *in situ* high-pulsed-power processing is used to explode emission sites (*rf processing*), thereby improving the cavity performance. Thermometric and microscopic results summarized here are used to develop a qualitative theory of the events leading up to rf processing. It is demonstrated that the ionization of gases from the emitter is crucial to the initiation of the explosion, similar to past observations made with dc emitters. This fact is underscored by the examination of emitters processed with intentionally administered helium gas in the cavity (*helium processing*). Numerical simulations of rf processing, including the ionization of gases by the field emission current, illustrate the conditions required for emitter explosion, and they confirm the importance of a plasma during such events. Most importantly, the calculations demonstrate that the positive space charge of the ions enhances the field emission current, and that the production of ions is a self-amplifying process. A runaway situation can ensue, which explains the submicrosecond rf-processing times observed experimentally. The rapid release of monolayer surface adsorbates at the emission site, in particular, can play a critical role in initiating voltage breakdown.

Keywords: Field emission; RF processing; Helium processing; Discharge; Voltage breakdown; Superconducting cavities

1   INTRODUCTION

A limit on the maximum accelerating gradient of superconducting radiofrequency (rf) cavities used in particle accelerators is imposed by the rf critical magnetic field.[1] Niobium cavities for e^+e^- accelerators are therefore limited to an accelerating gradient of about $50\,MV/m$. For a number of reasons, such high accelerating gradients are never achieved. The most common limiting mechanism is *field emission*.[1-3] In the presence of a high surface electric field, rf power is lost to electrons that tunnel out of the cavity wall at very localized points – usually from micron size conducting particles that contaminate the rf surface. The emitted electrons are accelerated by the electromagnetic fields, thereby absorbing rf energy. Field emission scales exponentially with the electric field and is capable of consuming substantial rf power.

Much effort is expended in cleaning superconducting cavities prior to their installation, to minimize particulate contaminants (and hence field emission). Nevertheless, not all emitters can be avoided in this manner. Further improvements in cavity performance can be achieved by applying high power to the cavity which can cause emitters to switch off abruptly (and permanently). This technique is known as *rf processing* or *conditioning*.[4] An understanding of processing thus is not only desirable for fundamental reasons, but also from a practical point of view, to permit its efficient application to cavities.

Similar conditioning events occur in dc gaps, and these have been examined extensively. DC high voltage studies with niobium and copper electrodes have shown that field emission is almost always a precursor to voltage breakdown, and that the breakdown event destroys the emitter (e.g. Refs. 5–7). The breakdown event is associated with a discharge and its accompanying plasma. Multiple (micron size) craters are frequently found at the site of the discharge.

Still, there are outstanding issues about rf-emitter processing by discharge. Is the mechanism in rf cavities the same as that for dc gaps? What is the chain of events that take place between emission and voltage breakdown? What conditions are needed for the formation of the discharge? For example, where does the gas for the discharge come from? Does the gas play any role in the field-emission process before breakdown? Certain emitters will process at a given

field, while others will not. What determines whether an emitter is processable?

Prior to these studies, we assumed that the Joule heating by the field-emission current alone is responsible for initiating the explosion. Thermometric and microscopic experiments with 1.5-GHz niobium cavities, described elsewhere in detail[8,9] and summarized here, proved this hypothesis to be wrong. The evidence suggests that a plasma can coexist with rf emission before the onset of the discharge, and that the ionization of gases evolving from hot emitters plays an important role in the progression of an emitter from steady-state emission to its explosion.

Another puzzle is the observation that large areas of the rf surface, many tens of microns across, can melt during the processing of an emitter, even though steady-state emission is from sub-micron regions.[8,9] In many instances, such regions are also surrounded by small secondary "satellite" craters. How does field emission continue after the microtip of the emitter melts? What produces the satellite craters? Again, we found that the plasma present during the discharge can explain such features.

When the field level is not sufficient to initiate a discharge spontaneously, it is possible to deactivate emitters by the intentional addition of helium gas in the cavity (*helium processing*). How does helium processing work? We were able to demonstrate, for the first time, that one important mechanism involves discharge. This discovery also emphasizes the important role played by gas during the transition from steady-state field emission to discharge.

Guided by such experimental findings, we developed new numerical simulations to model the electron-impact ionization of gases evolving from hot emitters. The simulations, described in some detail here, reveal some of the mechanisms underlying the discharge. Once a sufficiently dense gas builds up and large numbers of ions accumulate near the emitter, considerable electric-field enhancement results that leads to an instability in the emission current. A discharge is then created.

The improved understanding can account for certain characteristic features of discharge events, such as the occurrence of satellite craters at emission sites. Furthermore, our simulations set a time scale for the formation of discharge conditions.

2 EXPERIMENTAL EVIDENCE

2.1 Steady-State Emission and RF Processing

Thermometric and microscopic studies of field emitters in 1.5-GHz niobium rf cavities have revealed the following:[8-10]

1. Enhanced field emission, as described by the modified Fowler–Nordheim equation,[11] occurs primarily from microscopic tips ("microemitters") on conducting particles ("macroemitters") adhering to the rf surface. A combination of both geometric field enhancement *and* other (unexplained) mechanisms is responsible for an effective field enhancement of up to $\beta_{FN} = 1000$. Thus, field emission is observed at fields as low as 10 MV/m.
2. When the field-emission current density exceeds about 10^{11} A/m^2, the microemitters melt due to the Joule losses of the emission current. However, the complete extinction of a macroemitter cannot be explained by this local melting process alone.
3. If the current density is further increased (by raising the applied field), then the abrupt (and usually permanent) extinction of the entire macroemitter ensues.

Figure 1(a) depicts an electron micrograph of an active emission site that illustrates statement 1. The maximum current density recorded during the rf test was on the order of 10^{11}–10^{12} A/m^2. Localized melting of the particle is observed in the framed region magnified in
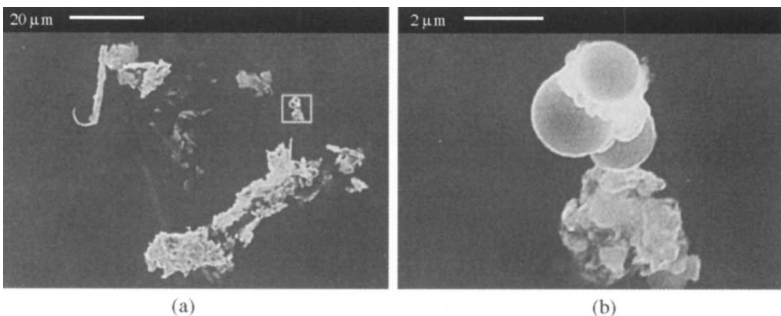

FIGURE 1 An active emission site located by thermometry in a 1.5-GHz niobium cavity. (a) Entire particulate region, (b) enlarged view of the framed region in (a). The main contaminants, as determined by energy-dispersive X-ray analysis, were iron, chromium, and nickel, suggestive of stainless steel.

Figure 1(b), consistent with statement 2. This observation also illustrates that the dominant emission takes place from small regions (microemitters) within the particle (the macroemitter).

Numerical estimates confirm that local melting by the field-emission current is possible at peak current densities on the order of 10^{11} A/m^2.[12] Similar observations were also made with dc field-emission experiments.[6,13-15]

Despite the melting of the microemitters, continued emission from the macroemitter in Figure 1 was observed during the rf test. Presumably several microemission sites were active.

The complete extinction (processing) of the particle does not take place until the entire macroemitter melts and explodes. An example of such an emitter is shown in Figure 2. Molten material, sometimes several tens of micrometers in radius, is found at the center of processed sites, surrounded by a large dark region called a "starburst"
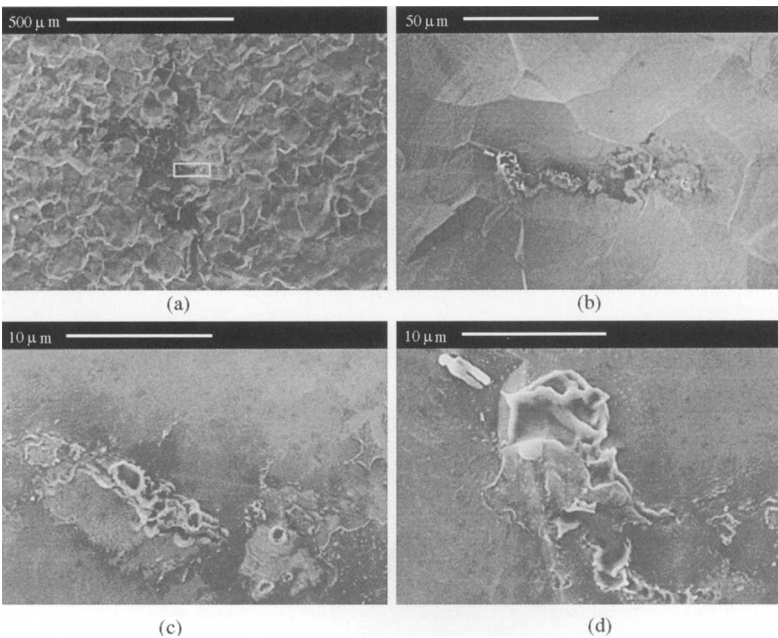

FIGURE 2   RF-processed emission site found in a 1.5-GHz niobium cavity. (a) Entire site. (b) Magnified view of the framed region in (a). Magnified views of (b) are shown in (c) and (d). The debris consisted primarily of carbon and oxygen. Only niobium was detected in the molten regions.

(see Figure 4 for a better example of a starburst). It is reminiscent of
an explosive event. Starbursts are a common feature of many pro-
cessed emitters. Sensitive Auger studies in the past have shown that
the starburst region is characterized by the *absence* of a thin layer of
fluorine (thickness $\geq 50\,\text{Å}$) that is present everywhere else on the cav-
ity surface.[16] Most likely, the fluorine is a remnant from the chemical
polishing used to clean cavities prior to testing.[8,9,17] According to the
current hypothesis, an extended plasma, produced by a discharge dur-
ing the explosion of the emitter, removes such surface contaminants,
thereby reducing the secondary-electron-emission coefficient in this
region.[16]

Consistent with the explosive characteristics of starbursts, one finds
that rf-processing events are very abrupt, lasting less than $1\,\mu s$. As an
example, the stored energy in a cavity during the application of a
60-kW, 120-μs rf pulse is depicted in Figure 3. The energy rose quickly
to $4\,\text{J}$ because of the strong external coupling to the cavity ($Q_e \approx 6 \times 10^5$). At that point, the peak electric field was $E_{pk} = 29\,\text{MV/m}$ and an
emitter processed. The processing event was accompanied by a brief
burst of X-rays. At the same, time the stored energy was drained in
less than $800\,\text{ns}$. Such rapid dissipation is inconsistent with a cavity
quench (*thermal breakdown*), which requires milliseconds.[19] Instead,
most of the power must have been dissipated in the field-emission
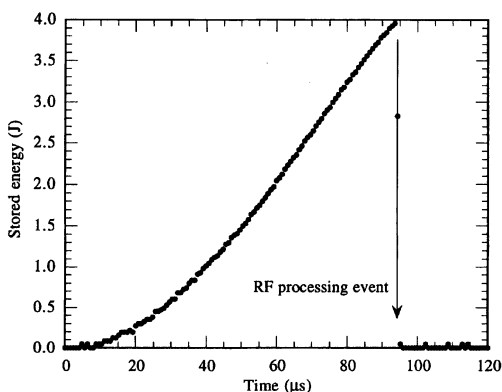current itself, draining, on average, a staggering $4\,\text{J}/800\,\text{ns} = 5\,\text{MW}$.

FIGURE 3   Stored energy during the application of a 60-kW, 120-μs rf pulse to a
1.3-GHz lead-plated copper cavity. A processing event was observed after about $95\,\mu s$
at a peak electric field of $29\,\text{MV/m}$. The external coupling to the cavity was 6×10^5.[18]
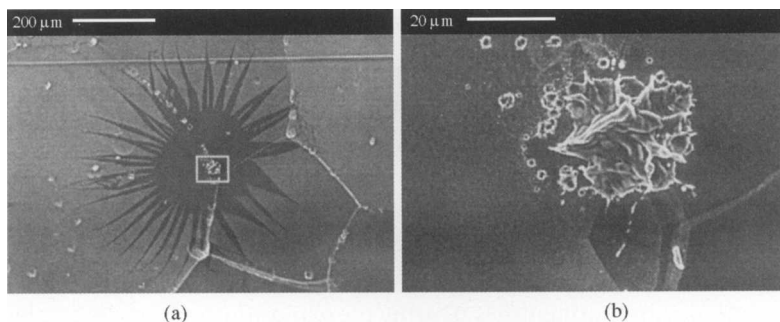
FIGURE 4   Field emitter that helium processed at $E_{pk} = 17\,MV/m$. (a) is magnified in (b). No foreign materials were detected by energy-dispersive X-ray analysis.

2.2   Helium Processed Emitters

Interestingly, the admission of small amounts of helium to the cavity (about $0.1-1$ mtorr, measured at room temperature), while applying rf power, can precipitate the abrupt extinction of emitters. This technique is called *helium processing*. Many field-emission sites processed in this manner have a very similar appearance to rf-processed emitters – that is, they are associated with a starburst and extensive melting at its center. Figure 4 depicts an example of such an emission site. *This emitter did not yield to rf processing up to the field level later used during helium processing.* Frequently, the main molten region is also surrounded by a number of secondary ("satellite") craters. The same applies to rf-processed emitters.

3   PROCESSING MODEL

3.1   Simple Model

The question now arises – how does an emitter process? What are the stages leading up to the destruction of an emission site?

A simple model is that the emission current's Joule losses simply melt and explode the macroemitter (see, for example, Refs. 4 and 12). RF processing thus takes place once the emitted current density exceeds a critical value. The starburst is created *as a result* of this

explosion. This simple model therefore involves three distinct stages:

1. *Pre-melting* At low fields, emission is active and degrades the cavity quality. The current density is insufficient to melt the emitter.
2. *Melting* As the electric field is raised, the current density increases exponentially. When it exceeds about $10^{11} \, A/m^2$, the emission tip begins to melt (see, for example, Figure 1(b)).
3. *Explosion* At even higher electric fields, the Joule losses of the emission current become so severe, that the entire macroemitter explodes and extinguishes. During the explosion, a plasma is created that produces the starburst.

This model brings up several questions. How does an emitter get from stage 2 to stage 3? How does emission stop? Why does helium gas precipitate the processing event? Calculations show that the melting due to steady-state emission (when the peak current density is about $10^{11} \, A/m^2$) is insufficient to melt more than $1 \, \mu m^3$ of the rf surface or large particles,[8,9] ruling out the creation of structures such as those in Figure 4(b). Still higher steady-state current densities are not possible, because space-charge effects limit the emitted current.[20-22] A reasonable assumption is that emission will cease when the microemitter melts because of the blunting of the microtip and the destruction of other field-enhancing mechanisms. Other tips on a macroemitter may continue to emit until they melt as well. However, unless all emission tips have the same effective field enhancement factor (β_{FN}), we would not expect them to melt simultaneously. Thus, rf processing should not be the abrupt event that is observed. Also, a processed emitter should consist of a series of molten tips, rather than a large mass of molten material as in Figures 2 and 4.

3.2 Improved Model

If the steady-state emission current is unable to melt large particles and large areas of the niobium surface, what is the source of the power dissipation?

When considering this question, *active* emission sites such as the ones shown in Figure 5 give a vital clue. Striking is the fact that a starburst exists in both cases despite the fact that the emitters did *not* process. Plasma activity must therefore play an important role in the final stages *before* rf processing.
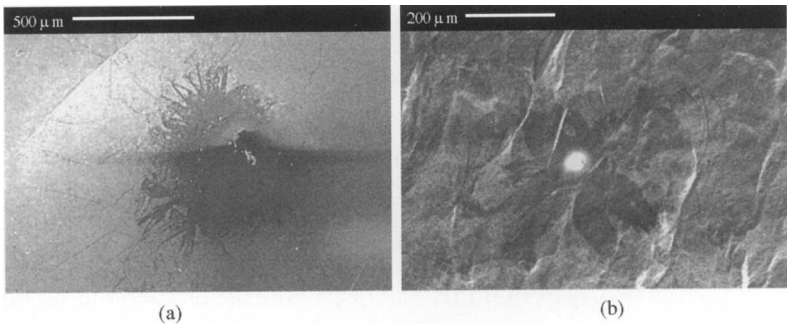
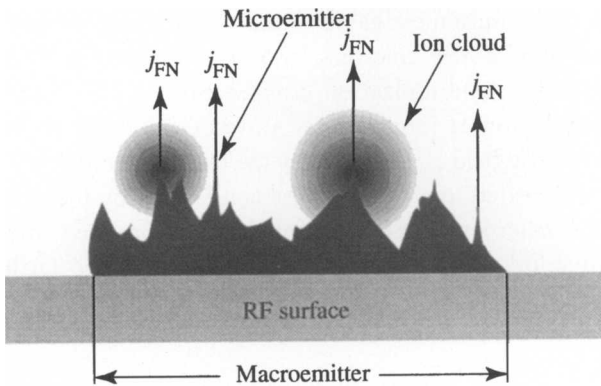FIGURE 5   Micrographs of two active emitters.

FIGURE 6   Schematic drawing illustrating a region of enhanced field emission (macroemitter) which is predominantly emitting from small areas within (microemitters). Due to the intense heating at the microemitters, gas is desorbed and is ionized by the emission current.

To explain the source of this plasma and its effect on the emitter, we propose to modify the three step model of the evolution of rf field emitters. A qualitative outline of the model is given here. In the next section we attempt to quantify certain aspects of this model with a simulation program called MASK.

Figure 6 illustrates schematically a field-emission site, similar to that shown in Figure 1. When the current density from a microemitter exceeds a threshold of about $10^{11} A/m^2$, it melts. The emitter in Figure 1 was at that stage when the rf test was ended. Near the melting temperature, neutral matter outgases or desorbs from the surface

and a gas cloud builds up in the vicinity of the emitter. Common adsor-
bates on superconducting cavity surfaces are water, hydrocarbons,
hydrogen, and carbon dioxide.[23] Material from the bulk of the melt-
ing microemitter will also contribute to this gas. The density near the
emitter depends critically on the temperature of the microemitter, the
surface condition of the emitter and the surrounding area, and its
response to deposited energy on submicrosecond time scales. Very
high gas densities are possible. If a single monolayer ($2 \times 10^{19}\,m^{-2}$) of
adsorbates is desorbed in 0.1 μs, the density at the emitter will be on
the order of $2 \times 10^{23}\,m^{-3}$ (at temperatures around 1000 K).

At typical field levels in cavities ($\approx 30\,MV/m$), emitted electrons
gain 30 eV within at most a micron of the rf surface. At this point,
they are able to ionize most gases. Almost all ionization occurs at dis-
tances less than a few microns from the rf surface, because the
product (gas density × ionization cross-section) is maximized in this
region.[a] The region of ionization is moved even closer to the rf sur-
face if the electric field is enhanced by the emitter geometry.

The newly created ions, in turn, are accelerated by the electric field
towards the macroemitter and, upon impact, produce further heat
and release more gas. This process provides positive feedback for
the gas evolution. If individual microemitters explode, the density is
further enhanced and a starburst may be produced even though the
macroemitter is still active.

The heavy ions move at most a few microns in one rf cycle. Conse-
quently, most are "trapped" near the emitter, leading to a rapid
buildup of positive space charge. Electric fields far in excess of the
externally applied field can develop, and a drastic enhancement of the
field-emission current results.

The positively charged cloud also serves to neutralize the increased
emission current, that otherwise is limited in magnitude by negative
space-charge effects.[20–22]

Given this revised model with additional new features, we find that
the plasma serves three primary purposes:

1. *Field enhancement*   The plasma enhances the electric field near the
   rf surface. The field-emission current, which scales exponentially
   with the electric field, is therefore augmented substantially. Since

---

[a] For most gases, the cross-section peaks between 15 and 100 eV.

the ohmic power dissipation increases quadratically with I_{FN}, the emitter temperature rises, and more neutral gas evolves and becomes available for ionization.

2. *Ion bombardment*   The ions are accelerated towards the rf surface and, upon impact, release even more gas and raise the emitter temperature.

3. *Charge neutralization*   The ions neutralize the emission current to eliminate space-charge effects that otherwise would limit the emission current density.

Critical to this model is the fact that it contains a positive feedback loop, as sketched in Figure 7, for the production of new ions. Once
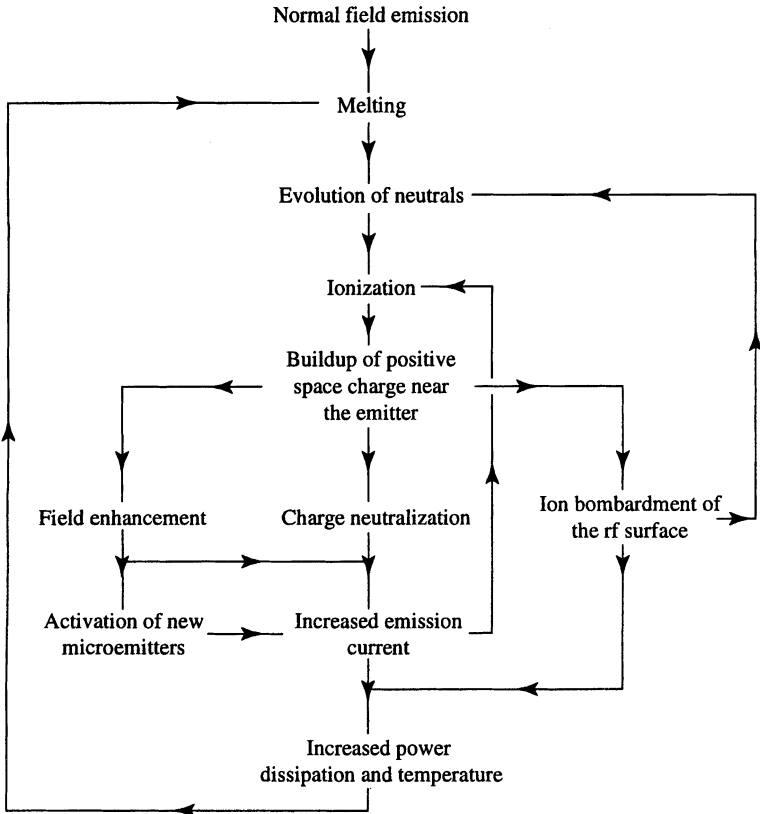

FIGURE 7   Flow chart of the feedback loop leading up to rf processing.

the rate of ion production becomes significant, the process is self amplifying and a rapid growth of the plasma density is expected.

Ultimately, the effect of the plasma is to dramatically increase the power dissipation in the field emitter, be it by field-emission Joule losses or ion bombardment. Eventually the entire macroemitter melts and explodes (rf processes). It is then no longer capable of enhanced field emission at the usual cavity operating fields.

The energy required to maintain this rapid plasma production and current growth is taken from the energy stored in the cavity fields. Hence, we always observe that the fields collapse during successful rf processing, as in Figure 3. In the next section, simulations will show that processing events can take place in much less than 1 μs!

3.3 Helium Processing Model

Based on this model, the helium processing of emitters, such as the one in Figure 4, can be readily explained.[8,9] Recall that this emitter did not yield to rf processing. Nevertheless, the micrographs in Figure 4 suggest that the mechanism responsible for helium processing is identical to rf processing. In some cases, rf processing may be limited by too little ion production, because either the neutral gas density or the emitted current (or both) is too low at the attainable field level. The admission of helium gas to the cavity increases the rate of ion production by augmenting the gas density (either directly or by additional ion bombardment). The emitter then is able to process.[b] The success of helium admission in triggering the explosion demonstrates the important role played by ions during rf processing.

4   COMPUTER MODELING OF RF PROCESSING

An analytical treatment of the processing model discussed previously is exceedingly difficult because of the many interdependent quantities involved in Figure 7. These problems are exacerbated by the fact that the region of interest is very small (10's of microns), yet includes all

---

[b] Other mechanisms for helium processing, which are non-destructive, have also been proposed.[8,11,24,25] They have been found to apply in some cases as well.

four states of matter, with very high temperature, density, and electric-field gradients. In addition to all this, rf-processing events are highly non-stationary.

A more fruitful approach is to simulate the process numerically using a discrete mesh to approximate the region of interest. Nevertheless, the task is formidable and many simplifying assumptions need to be made. The simulations discussed here were therefore only designed to yield order of magnitude estimates for the parameters describing the rf-processing mechanism.

For the most basic computations, a code is required that calculates the fields self-consistently. Essential, also, is the ability to include a neutral gas that can be ionized by the emission current. Fortunately, in our simulations the recombination of electrons with ions can be safely ignored because recombination rates at the plasma densities we encounter are much smaller than ionization rates.[8]

When considering the field-emission simulation problem, several length scales need to be addressed. They are discussed in the Appendix. Based on these considerations, a region a few tens of microns in size with a mesh spacing smaller than $0.5\,\mu m$ is sufficient for our simulations. No benefit is gained by simulating the entire cavity (which would be a monumental task). On the $10\,\mu m$ scale, the cavity fields, in the absence of field emission, are uniform[c] as in a parallel-plate capacitor.

Unfortunately, we are limited to time steps of about $dt = 10\,fs$ or less! This fact prevents us from simulating rf processing for more than a few rf cycles. Hence, in all cases our simulations are ended well shy of the ultimate processing event and are restricted to the ignition phase of rf processing.

4.1 Description of the Program MASK

We chose to simulate field emission using the code MASK running on an IBM RS/6000 workstation. The original version was developed by Science Applications International Corporation (SAIC). This FORTRAN code contained field solvers and particle-in-cell routines which could be employed "as is." Field-emission modules were already in existence as well.

---

[c] Provided we ignore the geometry of the field emitter.

Algorithms to permit the tracking of neutral particles and the ionization of these by electrons were added in collaboration within SAIC.

4.1.1 The Simulation Setup

A cylindrically symmetric parallel-plate arrangement (gap length d, radius R), as shown in Figure 8, was used for the simulations. The emitter is located on axis on the left plate. Because of rotational symmetry about the emitter, a two dimensional simulation in the $z-\rho$ plane suffices. The $z-\rho$ plane is divided into $m \times n$ mesh elements. The quantities relevant to the simulation, such as the electric field and charge density, are evaluated at discrete time intervals at various points on the grid. All quantities are assumed to vary linearly between grid points.

Both ions and electrons are simulated by discrete "macroparticles" (neutral particles are handled in a similar fashion). A macroparticle of charge $w_s Q_s$ and mass $w_s M_s$ represents w_s true particles of specie s each with charge Q_s and mass M_s. The "weights" w_s are chosen so that the total number of macroparticles in the simulation is computationally manageable. Generally, MASK can cope with several 10,000 macroparticles at a time. It is desirable to have more than one macroparticle in each mesh element, within the region of interest.
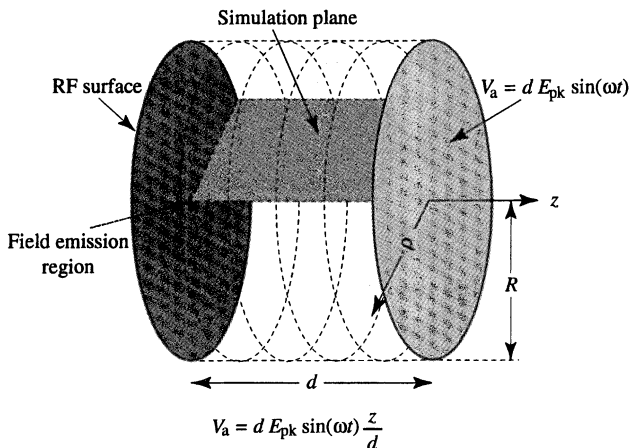

FIGURE 8 Parallel-plate capacitor arrangement used to simulate rf processing in cavities.

4.1.2   Electric Field

The externally applied field is spatially uniform. Hence, an oscillating potential V_a was applied to the right boundary at $z = d$. The left boundary, on which the emitter is located, was grounded (0 V). On the remaining side (along $\rho = R$) a linearly increasing potential between 0 V at $z = 0$ and V_a at $z = d$ was imposed. In all cases the applied potentials were allowed to evolve as

$$V(t) = V_a \sin \omega_0 t, \tag{1}$$

where ω_0 was either $2\pi \times 1.5\,\text{GHz}$ or $2\pi \times 5\,\text{GHz}$.

Any charges in the simulation region are taken into account by the field solver when calculating the electric field. Particles that cross the boundaries are discarded. Hence the choice of d and R influences the outcome of the simulation in two ways; the field distribution is altered because of the artificially imposed boundary potentials along $z = d$ and $\rho = R$, and charges which cross boundaries no longer contribute to the source terms. However, we found that for $R \geq 8\,\mu\text{m}$ and $d \geq 32\,\mu\text{m}$ the boundaries only had a small effect on the outcome of the simulation.

The magnetic field was not included in the calculations, because the electric forces far outweighed the magnetic forces.[8] Magnetic forces would become significant if the simulations could be carried on further into the processing stage. Future simulations therefore must account for magnetic effects.

4.1.3   Modeling Field Emission

The field-emissive area, radius r_{em}, is located on axis on the left boundary. Particulate features were not included and therefore no geometric enhancement of the electric field occurs.

The emitted current density is given by

$$j_M = \begin{cases} A_M E_{em}^2 \exp(-B_M/|E_{em}|) & \text{when } E_{em} < 0 \\ 0 & \text{when } E_{em} \geq 0, \end{cases} \tag{2}$$

where E_{em} is the electric field at the emission site, and A_M and B_M are constants supplied by the user. They are adjusted to yield currents comparable to those observed in niobium cavities.
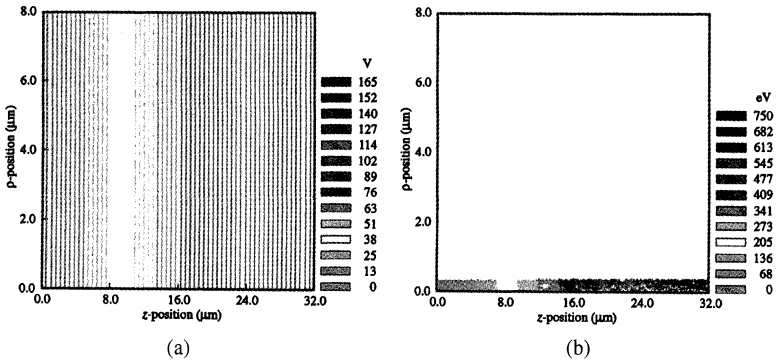
FIGURE 9 Typical simulation setup: (a) Potential distribution in the simulation region due to the uniform, externally applied, electric field. (b) Injection of the field-emission current into the simulation region. The color denotes the electron energy. In the depicted case, the current's self field is significantly less than the externally applied field. Note that the aspect ratio is not 1 : 1 in these figures. (See color plate I).

Figure 9(a) shows the potential distribution within the simulation region in the absence of significant numbers of charges. Similarly, Figure 9(b) depicts the injected field-emission current which, in the case shown, is sufficiently low so that its self-field is not apparent.

4.1.4   Neutral Particles

Neutral macroparticles can enter the simulation region from any point. The motion of these particles ("neutrals") is tracked by MASK. To simulate the gas evolving from a near-molten emitter, we injected neutrals from a region, radius $1\,\mu m$, centered on the emission site. This size seems reasonable based on the molten microemitters in Figure 1(b). The injection of neutrals was modeled on the effusion of gas from a Knudsen cell.[26] The resultant flux distribution has a $\cos\theta$ profile, where θ is the angle to the normal of the rf surface.

As an example, consider the effusion of 2000 K magnesium neutrals. For a flux of $10^{27}\,m^{-2}\,s^{-1}$ the steady-state neutral gas density near the emitter, as calculated by MASK, is shown in Figure 10.[d] Although this flux is high, we will see later that considerably lower gas densities still trigger rf processing.

---

[d] From the ideal-gas law, the gas density at the emitter should be $3.1 \times 10^{24}\,m^{-3}$. The discrepancy is probably due to the finite size of the mesh elements and the limited number of macroparticles that can be used in a simulation.
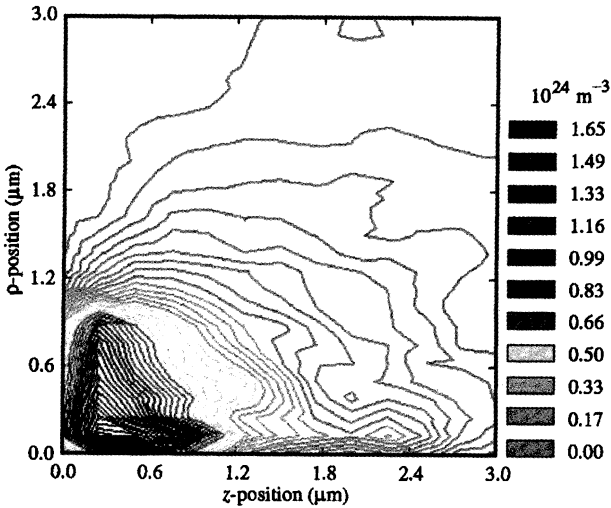
FIGURE 10   Density of magnesium gas effusing from the 1 μm region centered on axis at the left surface. The flux was $10^{27}\,\mathrm{m}^{-2}\,\mathrm{s}^{-1}$ and the temperature of the effusing gas was 2000 K. Only the immediate vicinity of the field emitter is shown. (See color plate II).

4.1.5   Ionization

The neutral gas in the simulation region is subject to electron-impact ionization by the field-emission electron beam. Given the neutral gas density and the electron density, as well as the average electron velocity in each mesh element, MASK is able to estimate the ionization rate. The cross-section data as a function of electron-impact energy for several elements was programmed in MASK (see Figure 11). Based on the ionization rate, the code continuously adds positive ions to the simulation region. These constitute additional source terms when computing the electric field.

Note that the cross-section for many of the materials commonly found at field emitters in cavities – for example, iron, indium, copper, and titanium – are very similar. Magnesium has been found in cavities on occasion as well, but not as frequently. Many of our simulations were carried out with magnesium as the neutral gas. However, the actual gas species being used has little bearing on the outcome of the simulation. Magnesium should thus be viewed as a generic gas that can be replaced by any of the common metals found in cavities.
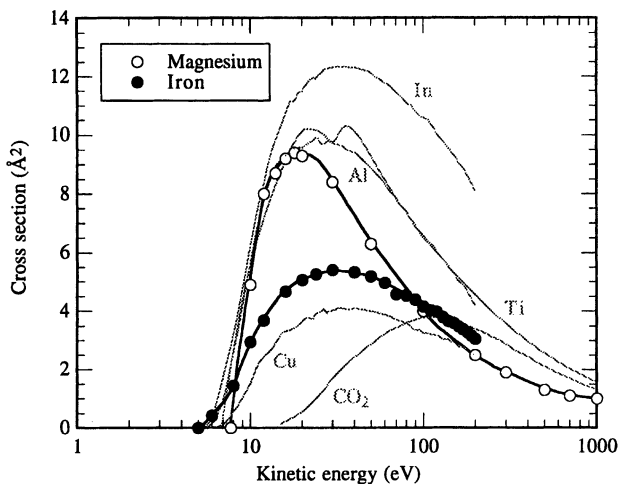
FIGURE 11   Total electron-impact-ionization cross-section data for magnesium,[27] iron, copper, indium, aluminum,[28] titanium,[29] and carbon dioxide.[30] The cross-sections for iron and magnesium were used in MASK simulations. The others are included for comparison to illustrate that within an order of magnitude little differences exist.

4.1.6   Validation using Towsend Discharge

Past tests have shown that simulations using MASK field solvers and charged particle routines agree with experimental results.[31,32] The ionization and neutral-particle routines were only recently added and still needed testing. Towsend discharge,[33] which has been the subject of extensive experimental studies, was an obvious candidate for such tests because of its apparent similarity to our field-emission simulations. Results reported on in Ref. 8 demonstrated that the agreement between simulations and experimental Towsend data is sufficiently accurate to give us confidence in the field-emission simulations described next.

5   FIELD-EMISSION SIMULATIONS

The following description of a simulation run (requiring about four hours of computing time) is a generic example of all our simulations that led to rf processing. The qualitative (and, to a large extent, quantitative) results are common to most of our simulations.

5.1   Simulation Parameters

We chose an applied field of 30 MV/m at a frequency of 5 GHz. The size of the region studied was $32 \times 8 \, \mu m^2$ and the mesh density was 128 elements $\times$ 64 elements. The time step was $dt = 10 \, fs$.

The parameters chosen for the field emitter were

$$A_M = 4.13 \times 10^9 \, A/MV^2, \tag{3}$$
$$B_M = 218.5 \, MV/m. \tag{4}$$

The radius of the field emitter was 2 mesh elements ($r_{em} = 0.25 \, \mu m$). This is probably a little larger than real microemitters, but a reduction in size is difficult because of the corresponding increased computational burden due to the finer mesh requirement.

Given A_M, B_M, and r_{em}, the total peak current according to (2) is $I_M = 0.5 \, mA$ at 30 MV/m, and the peak current density is $j_M = 2.5 \times 10^9 \, A/m^2$.

The gas flux was $10^{27} \, m^{-2} s^{-1}$ at 2000 K. The flux is higher than that used in later simulations, but the results illustrate well the effect of the ion production on the emission process. A reduction of the gas pressure does not significantly change the qualitative results, except that longer simulation times are required.

5.2   Simulation Results

Initially, at low field, the emission current enters the cavity as a pencil beam (see Figure 9(b)). Ions are produced in the region where the product of the ionization cross-section and the gas density is maximized, i.e., within a few microns of the rf surface. The ions do not move far in an rf cycle and accumulate near the emitter. After $1\frac{1}{4}$ rf cycles (25,000 time steps) a significant number of ions have already been created, as shown in Figure 12. The peak ion density is on the order of $2 \times 10^{22} \, m^{-3}$.

5.2.1   Ion Field Enhancement

In Figure 12 the applied electric field is at its peak, i.e., at 30 MV/m. The positive charge near the emitter enhances the rf field further, so that the total field exceeds 30 MV/m. In Figure 13(a) one finds that the equipotentials near the ion cloud are distorted. The corresponding
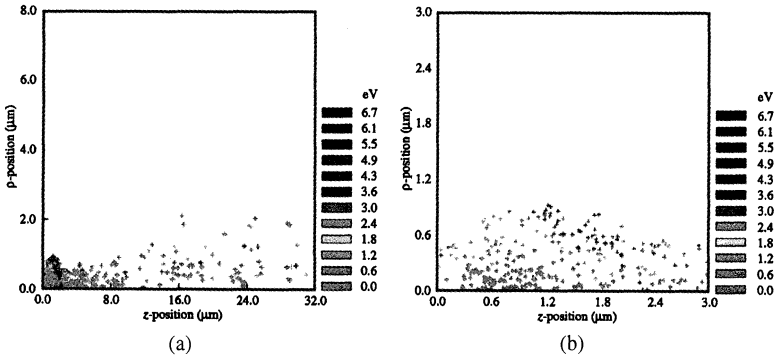
FIGURE 12   Position plots of the ions after $1\frac{1}{4}$ rf periods. Each cross represents 10 ions. The color indicates the ion energy. (a) The entire simulation region – note that the aspect ratio is not $1:1$. (b) Magnified view of the $3 \times 3\,\mu m^2$ region closest to the emitter. (See color plate III).

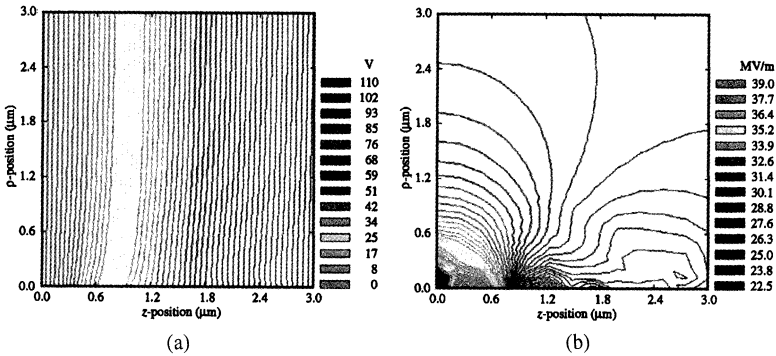FIGURE 13   Contour plots of (a) the scalar potential and (b) $-E_z$ within the $3 \times 3\,\mu m^2$ region closest to the emitter. Both "snapshots" were taken $1\frac{1}{4}$ rf periods into the simulation. (See color plate IV).

electric field in the z direction is as high as $39\,MV/m$ (Figure 13(b)), even in the presence of the emission current's space charge.

Due to the enhanced electric field, the emission current increases (we will return to this point later). As the current leaves the emission site, the radial electric field due to the ions "focuses" the electron beam within a few microns of the rf surface (see Figure 14). This effect serves to further concentrate the ion production in the high-density gas region. Once the beam emerges from the ion cloud, its own space charge causes it to spread significantly.
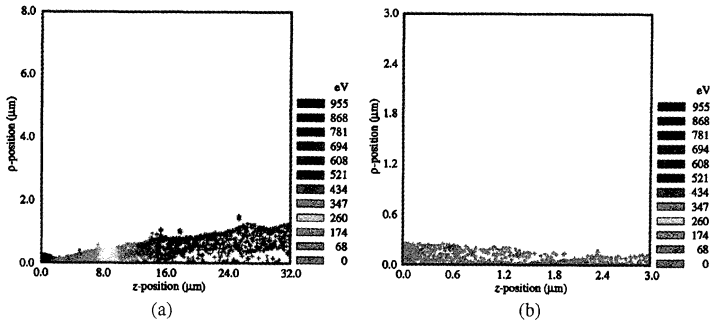
FIGURE 14   Position plots of the electrons $1\frac{1}{4}$ rf periods into the simulation. (a) The entire simulation region – note that the aspect ratio is not $1:1$. (b) Magnified view of the $3 \times 3\,\mu m^2$ region closest to the emitter. In both cases the electron energies are given by the color of the crosses. (See color plate V).
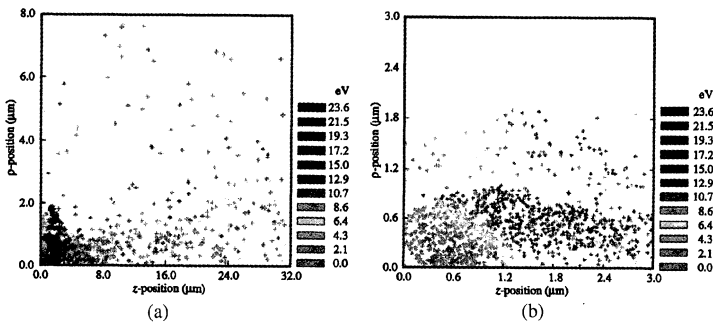

FIGURE 15   Position plots of the ions after two rf periods. Each cross represents 10 ions. The color indicates the ion energy. (a) The entire simulation region – note that the aspect ratio is not $1:1$. (b) Magnified view of the $3 \times 3\,\mu m^2$ region closest to the emitter. (See color plate VI).

As the simulation progresses through the half of the rf cycle when the applied field inhibits field emission, the ions slowly begin to spread. They move a distance on the order of 1 μm. Ions heavier than magnesium (e.g., iron and indium) will move even less. Hence, by the time the third rf cycle begins, many of the ions are still in the vicinity of the emitter (Figure 15). The applied electric field at this time is zero, but the field due to the ions is as high as 25 MV/m (see Figure 16). Hence, electrons are being drawn from the emitter and are trapped in the ion cloud (Figure 17). A plasma is created.
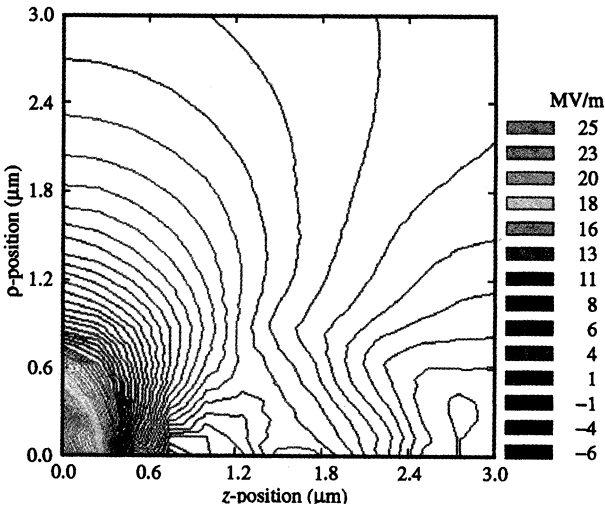
FIGURE 16   Contour plot of $-E_z$ near the field emitter at the beginning of the third rf period. The applied rf field is zero at this point in time. (See color plate VII).
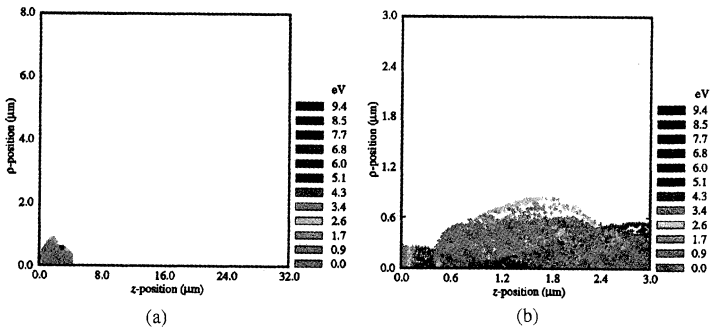

FIGURE 17   Position plots of the electrons at the beginning of the third rf period. (a) The entire simulation region – note that the aspect ratio is not 1:1. (b) Magnified view of the $3 \times 3\,\mu m^2$ region closest to the emitter. Clearly visible is the injection of emission current from the rf surface despite the fact that the externally applied field is zero. (See color plate VIII).

By the time the simulation has advanced another 1/4 rf cycle, the plasma has nearly expelled the electric field from its interior (Figure 18(a)). The density is on the order of $10^{23}\,m^{-3}$. A potential drop between the plasma and the rf surface develops to impede the flow of the more mobile electrons back to the rf surface, so that
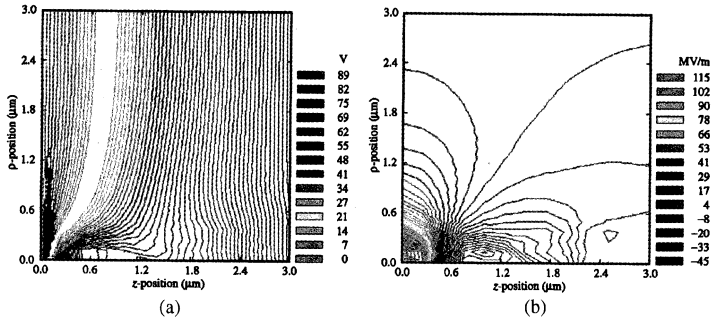
FIGURE 18 (a) Equipotentials near the field-emission site after $2\frac{1}{4}$ rf periods. (b) Contour plot of $-E_z$ at the same time. The field enhancement due to the plasma near the rf surface is very apparent. (See color plate IX).

charge neutrality is preserved (*sheath formation*[34]). The field in the sheath is nearly 120 MV/m, far in excess of the applied field of 30 MV/m at that time (Figure 18(b)). Shortly after this point in time, the simulation was halted because the resolution of the mesh was insufficient to yield accurate results at such high electric fields.

5.2.2 Evolution of the Emission Current

Figure 19 depicts the field-emission current as a function of time for the first $2\frac{1}{4}$ rf cycles. Included is the simulated current under identical circumstances if the neutral gas is omitted from the calculations. In the latter case, the current never attains the 0.5 mA level predicted by (2) because of space-charge limitations.[e] In contrast, the current rises rapidly when the gas is included and ionization takes place. Both the ion-enhanced electric field and the neutralization of the electron current contribute to this effect.

Within just over two rf cycles the peak current has risen from 44 μA to over 10 mA – a 227 fold increase.[f] Not only does the peak current rise, but the fraction of each rf cycle during which field emission is active also increases, since the ions tend to provide a dc bias to the

---

[e] Space-charge effects are not expected to be quite as severe for emission from real emitters because the macroemitter geometry enhances the applied electric field.

[f] In fact, we had to impose an artificial field-dependent limit on the emission current to prevent unphysical instabilities due to the discrete simulation time steps. In the absence of this limit, the current increase might have been even greater. See Ref. 8 for more details.
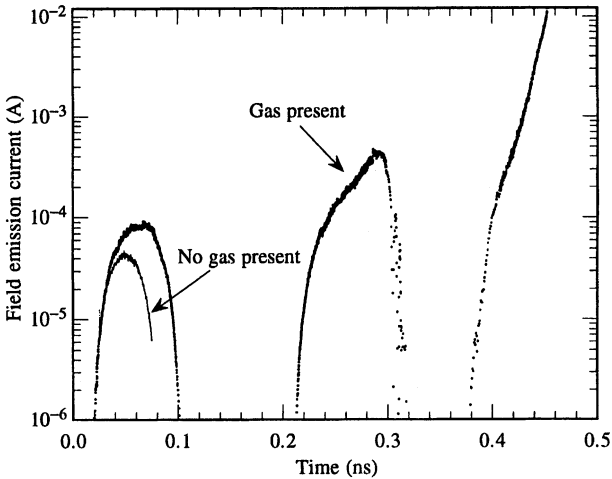
FIGURE 19   Emitted electron current versus time for a simulation including a neutral gas and the same simulation with no neutrals present.

applied rf field. Hence, the average current rises even faster than the peak current.

5.2.3   Power Dissipation

Due to the resistivity of the emitter, the emission current causes Joule losses.[g] Since the emission current increases rapidly as the ion cloud develops, the time-average Joule losses also rise dramatically. Conservatively, one would expect the dissipated power to scale quadratically with the peak current. Hence, the dissipated power will increase at least by a factor of $227^2 = 5.2 \times 10^4$ due to the presence of the gas.[h] In turn, the increased dissipation will drastically raise the emitter temperature and result in the effusion of substantially more gas which becomes available for ionization – a fact that was *not* included in this particular simulation. The ionization process, hence, is part of a positive feedback mechanism, as was anticipated in the previous section.

---

[g] Note that throughout this article we have assumed implicitly that the initial current density is sufficient to heat the emitter and cause the release of the neutral gas used in the simulation.

[h] An even greater factor should be used, considering that the time-average emission current rises faster than the peak current.

5.2.4   RF Processing

Unless there is some mechanism to limit the current growth, this type of field emission must end in an explosive event (rf processing). For practical purposes, we deem an emitter as beginning to rf process if the emission current in the simulation exceeds the (somewhat arbitrary) threshold of 0.01 A, i.e., when the rapid current growth (as during the third rf cycle in Figure 19) has been well established. We expect that eventually the heating of the rf surface due to the augmented current or ion bombardment (to be discussed later) becomes so severe, that the macroemitter is heated far above its melting point and explodes. This prediction is consistent with theories of dc discharge, where temperatures in excess of 10^4 K have been encountered in times as short as 1 ns.[5,35] Later, we will show that field emission can continue even after the microemitters melt, provided a significant number of ions are already present nearby.

Ultimately, the energy stored in the cavity sets a limit on the maximum possible current that can be emitted. Any charge absorbs energy from the cavity fields as it is accelerated before impacting the cavity walls. At the impact sites, the rf surface temperature is raised and more power is absorbed, perhaps even leading to a quench. In any case, field emission must cease once the cavity energy has been drained (Figure 3).

Our simulation predicts that an explosion will take place within a small number of rf cycles. At lower gas densities, the time to explosion is longer, but nevertheless is on the order of several rf cycles. We assumed that at the beginning of the simulation the neutral gas density near the emitter, in particular within the first few microns, has already been established. At gas temperatures on the order of 1000 K, neutrals move about 1000 m/s. Hence the gas requires 5 ns to travel 5 μm. In addition, one needs to take into account the time it takes to substantially heat the microemitter itself. Calculations have shown that a field emitter can melt niobium within as little as 1–100 ns, provided the current density is high enough.[12]

The total time to rf process an emitter (t_{proc}) is thus given by

$$t_{proc} = t_{heat} + t_{gas} + t_{expl}, \qquad (5)$$

where t_{heat} is the time taken to heat the emitter to release the gas, t_{gas} is the time required by the gas to move a few microns, and t_{expl} is the

time until an explosion takes place. Given the time scales discussed above, we can expect an emitter to rf process in a time on the order of a few nanoseconds to a microsecond. These times are consistent with processing times like those observed in Figure 3 where, on average, the current dissipated *at least* $4\,J/800\,ns = 5 \times 10^6\,W$.

Typically, in L-band cavities, field emitters (prior to rf processing) dissipate anywhere between ten and several hundred watts of power at currents around $0.5\,mA$.[i] Taking $100\,W$ as a reasonable value, we find that an estimate of the emission current *during* the processing event is given by $(5 \times 10^6\,W/100\,W) \times 0.5\,mA = 25\,A$! Peak currents may even be considerably higher, especially if the rf processing event takes significantly less than $800\,ns$. Of course, this simple estimate ignores items such as space-charge effects, since we simply scaled the power dissipated by the cavity field in the emission current linearly with the magnitude of the current. However, the estimate does illustrate that enormous currents are feasible during rf processing.

Since the maximum current recorded in our simulation was only $10\,mA$ we see that our calculations were ended long before the ultimate processing event. Reference 7 describes four stages of dc breakdown: pre-breakdown, ignition, current growth, and arcing. Steady-state rf field emission is to be compared with dc pre-breakdown. Our simulations then enter the ignition phase and the beginning of the current growth phase, but are stopped long before the maximum current is ever achieved.

Sub-microsecond processing times have also been observed in pulsed dc vacuum-discharge experiments.[5,14,36,37] Pre-breakdown currents in dc discharge experiments are in the $0.1-10\,mA$ range,[14,38] comparable to rf field emission. During the dc breakdown phase, currents from 1 to $100\,A$ have been recorded.

5.2.5   Plasma Density

By the end of the simulation, ion densities have risen to $\approx 3 \times 10^{23}\,m^{-3}$. For transient plasmas, these densities are not unrealistic and densities as high as $10^{26}\,m^{-3}$ have been observed in cathode flares,

---

[i] This is the power dissipated when the emitted charges are accelerated by the cavity fields, not the Joule losses.

which are created at the cathode during explosive dc field emission.[5,13,36] It is likely that the plasma densities observed during our simulations constitute a lower bound on the densities that occur during rf processing.

5.3 Critical Gas Density

The qualitative features of the results described above are common to *all* our simulations that led to rf processing. Nevertheless, parameters such as the neutral gas density, r_{em}, A_M, B_M, the applied field, and the rf frequency impact the quantitative aspects of a simulation. So far we have only explored a limited region of this parameter space.

Of particular interest to us was the determination of the gas density required at the outset of the simulation to initiate rf processing. The simulation described above used a fixed gas density of about $2 \times 10^{24}\,\mathrm{m}^{-3}$, which is fairly high. Our objective was to determine whether such high densities are necessary and, if not, we wanted to find a reasonable estimate of the lowest possible *initial* density required for rf processing. We call this threshold value the "critical density." Once known, the critical density can then be used to determine whether such values are feasible near cavity emission sites.

Our simulations demonstrated that successive reductions of the gas density in the simulations by factors of 1/2 quickly eliminate the explosive behavior.[8] Based on these results, critical densities on the order of $10^{24}\,\mathrm{m}^{-3}$ are predicted.

However, we already pointed out that the gas density at real emitters increases whenever the dissipated power is augmented. When this effect is included (to a limited extent), we find that predicted densities are lowered dramatically – to between 3×10^{20} and $3 \times 10^{22}\,\mathrm{m}^{-3}$. A comparison of these densities with the vapor pressure of common emitters shows that such values are feasible near real field emitters. (See Ref. 8 for more details.)

A number of other factors, not included in the simulations, affect the critical gas density. In all cases we are led to believe that the true critical density is even lower than our predictions. For example, space-charge effects due to our inability to simulate the macroemitter geometry limited our steady-state emission currents to about 1/10 of measured currents. To compensate, initial gas densities in the

simulations need to be about 10 times higher to initiate processing. Geometric field enhancement also moves the region of dominant ionization (determined by the electron energy) closer to the rf surface (and into regions of higher gas density). Again, the computed critical density is overestimated due to the omission of the emitter geometry. Mesh-size considerations also forced us to use current densities lower than expected with real emitters. Reduced ion densities result, raising the critical gas density once more. Finally, we also ignored the desorption of adsorbates due to the ion bombardment and heating of the rf surface, so yet again the critical density is overestimated. We believe that this desorption process, in particular, may be a significant source of gas.

5.3.1   Surface Composition and Ion Bombardment

In all our simulations, the gas density was compared with the vapor pressure of the heated emitter. In reality the composition of the rf surface may play an important role, and the use of the metal vapor pressure constitutes, at best, a lower limit on the gas pressure. The true gas density will depend critically on the condition of the first few monolayers of the emitter and the surrounding rf surface, and how these layers react to deposited energy on nanosecond time scales. Studies have shown that the niobium rf surface is covered by several monolayers of hydrocarbons, water, and fluorine ($>50 \, \text{Å}$)[16], and the oxide layer is $60 \, \text{Å}$ thick.[39] Hydrocarbons, in particular, are physisorbed and can be desorbed reasonably easily. Adsorbed hydrogen at cryogenic temperatures is also common. If one monolayer (areal density $2 \times 10^{19} \, \text{atoms/m}^2$) is released over a period of 500 rf cycles (at 5 GHz), then over this short time scale the gas density at the emission site will rise to a density on the order of $2 \times 10^{23} \, \text{m}^{-3}$. This density already exceeds the critical density we obtained from MASK simulations.

Even though the ions do not move very far in one rf cycle, they can gain several hundred eV, especially if the electric field is enhanced by the emitter geometry. Upon impact with the rf surface, they are capable of releasing neutral atoms, secondary ions, and electrons. For clean target surfaces, neutral-particle yields do not exceed a few atoms per ion up to ion energies around 100 eV.[40–42] Little information is available on the secondary neutral-particle yield for cryogenic targets

covered by adsorbates we commonly encounter in superconducting cavities. One study revealed that for one monolayer hydrogen coverage of copper, the yield of H_2 molecules can be as high as 10^4 molecules/ion when sputtered by 5-keV H^+ ions.[43] Even 2-keV electrons were able to sputter close to 10^3 molecules/electron.

In our MASK simulations, we found that for an initial gas flux of $10^{25}\,m^{-2}s^{-1}$, about 320 ions impacted a region radius 0.4 μm centered on the emitter during the 1/2 rf period (at 1.5 GHz) while field emission was active. The simulation was carried out at an applied field of 120 MV/m to mimic macroemitter field enhancement. The peak impact energy recorded was 800 eV, the mean energy being 200 eV. The average power flux into the area was 31 MW/m². If each ion releases only 10 adsorbate molecules, then the increased molecular flux during that half rf cycle is 10 neutrals/ion $\times$ 320 ions $\times 3 \times 10^9\,s^{-1}/\pi(0.4 \times 10^{-6}\,m)^2 = 2 \times 10^{25}\,m^{-2}\,s^{-1}$. This value exceeds the original flux used in the simulation by a factor of 2! The desorbed material will move at velocities up to 1000 m/s. Hence, after only one or two rf cycles the desorbed gas will have traveled to the point where the electrons have the optimal energy for ionization.

Once a dense plasma is formed, the rate of ion bombardment increases even further. Figure 20 depicts a situation where the acceleration of ions in the sheath between the plasma and the rf surface is clearly visible. Not only will these ions sputter neutral matter, but they also contribute to the power dissipation at the emission site. In the situation depicted in Figure 20, the average power dissipation from $\rho = 0$ to $\rho = 0.5$ μm was 2×10^{10} W/m². This value only considers the kinetic energy of the ions and neglects the energy released when ions and electrons recombine at the rf surface.

In contrast, the power dissipated by the field-emission current per unit area is approximated by

$$\frac{dP_{FN}}{da} = \bar{j}_{FN}^2\, \rho l, \qquad (6)$$

where l is the distance traversed by the emission current in the rf surface of resistivity ρ and $\bar{j}_{FN}$ is the time-average emission current. For lack of any concrete numbers, we shall assume that l is comparable to the size of a microemitter, i.e., $l \approx 0.5$ μm. If $\bar{j}_{FN} = 10^{11}\,A/m^2$ and
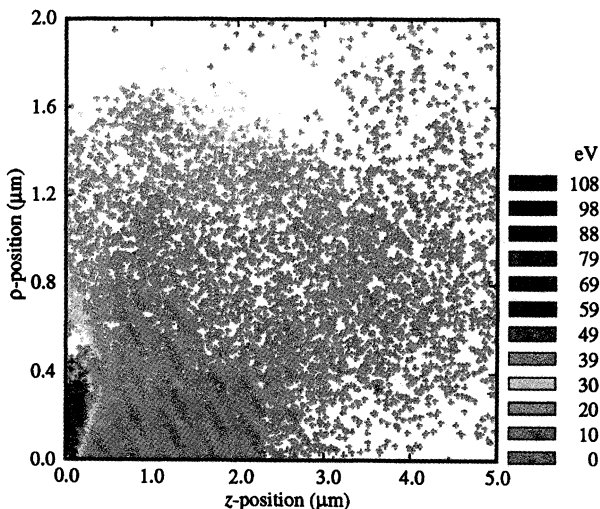
FIGURE 20   Ion bombardment of the rf surface once a plasma has been established near the emitter. The ions are accelerated by sheath field between the plasma and the rf surface. Applied field = 30 MV/m. Note that the aspect ratio is not 1 : 1. (See color plate X).

$\rho = 10^{-6}\,\Omega$m, one finds that[j]

$$\frac{\mathrm{d}P_{FN}}{\mathrm{d}a} = 5 \times 10^9 \,\mathrm{W/m^2}. \tag{7}$$

Hence, the power dissipated by the bombarding ions even this early into the rf processing sequence exceeds the Joule heating by the steady-state emission current.

Ion bombardment therefore is likely to play an important role in triggering rf processing. Not surprisingly, the initiation of dc break-down is observed to be very sensitive to the surface state of the elec-trodes.[7] Hence, it is important to gain more insight into the composition of the rf surface following standard cavity treatment techniques. In particular, adsorbate effusion rates from the rf surface over very short time spans need to be known as a function of local-ized energy dissipation and ion-bombardment rates.

---

[j] $10^{11}\,\mathrm{A/m^2}$ is the maximum time-average steady-state current density to be expected from rf-cavity emitters.

5.4 "Natural" Field Emission

Irrespective of the initial critical gas density required for rf processing, we have shown that the plasma which forms near the emitter produces a substantial electric field at the rf surface.

Figure 21 demonstrates the enormous fields that are possible. Even though the externally applied field at this time was a mere 28.7 MV/m, the field at the emission site exceeds 1000 MV/m! Even six emitter radii out from the symmetry axis the electric field is 60 MV/m, more than twice the applied field. Greater fields probably occur, if the simulation did not have to be ended at this point in time due to the inadequate mesh size.

This result demonstrates that nearby microemitters will become active, even if their effective field enhancement factor (β_{FN}) is low. A relatively large area is now capable of emission and a very large current can be drawn at low current density (thereby bypassing space-charge limitations). These large currents are then responsible for further neutral gas release and ion production. The plasma cloud is thereby extended to envelop other parts of the macroemitter. Ultimately the entire macroemitter may emit.

It is also important to note that on axis the electric field exceeds 1 GV/m. At these field levels "natural" field emission becomes
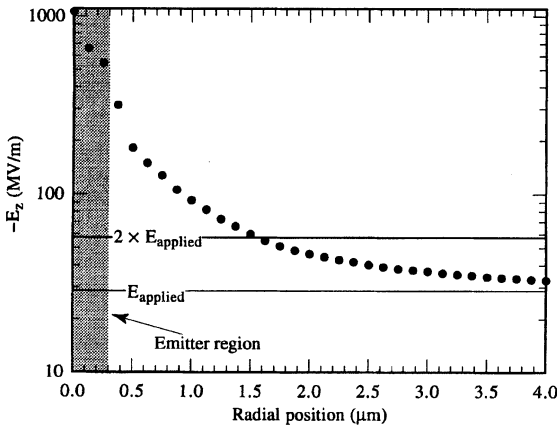

FIGURE 21 $-E_z$ versus radial position along the rf surface at the end of a simulation leading to rf processing. The field-emission current was "turned off" shortly before this point in time to eliminate its space charge. Note the semilogarithmic scale.

possible. The term "natural" implies that only simple geometric field enhancement ($\beta_{FN} \leq 10$) is required for strong emission. This type of emission is to be contrasted with "enhanced" field emission with $\beta_{FN} = 100 \rightarrow 500$ commonly found in cavities, which requires non-geometric enhancement mechanisms to achieve such high β_{FN} values.[1,3,44] At fields on the order of a few GV/m, even a perfectly smooth (possibly molten) sphere or bumps in the niobium rf surface will emit. If the ionization process is permitted to continue beyond the end of our simulations, local fields on the order of 5 GV/m may be possible, at which point even a flat niobium surface field emits (and, more importantly, begins to melt due to the emission current). The field-emission process at this time is no longer reliant on the presence of foreign particulates on the rf surface. We expect, therefore, that field emission progresses beyond the melting stage of the original microemitter and does not cease until all stored energy in the cavity is dissipated in the rising current (as in Figure 3), regardless of the fact that the original microemitter may no longer be capable of emission in the absence of a plasma.

5.5 Satellite Craters

So-called satellite craters, which often surround emission sites in rf cavities (see Figure 4(b)) and in dc gaps[45], are also explained by this mechanism. Small defects or particulates are likely to exist in the vicinity of a macroemitter and act as emission centers once the plasma from the central emission site envelopes them. Their explosion can lead to satellite craters. Ejected drops from the central site will also serve as emission centers. Microtips can also be created due to stretching of liquids in the presence of a strong electric field and have been observed in dc field emission.[46] All these features are potentially powerful field emitters, *provided they come into contact with the plasma.*

6 SUMMARY OF THE PROCESSING SEQUENCE

To conclude, we reiterate the salient facts of rf processing deduced from the simulation results presented here. These features are common to all our simulations.

   In the absence of any ionizable gas, we found that the emission current does not exceed a fairly low value (44 μA), despite the fact that the theoretical current given by Eq. (2) may be significantly higher (500 μA). The self-field of the emission current is responsible for this discrepancy. Steady-state currents from real cavity emitters have been observed at the 500 μA level. Such high currents are probably attained with the assistance of geometric field enhancement by the macro-emitter. Nevertheless, the heating due to such currents alone is incapable of exploding an entire macroemitter. Because of space-charge limitations, we suspect that even higher steady-state currents cannot be achieved.

   The situation changed drastically when the ionization of gas evolving from the emitter was included in the simulation. Both the outgassing of hot emitter material and the desorption of adsorbates contribute to this gas. Ions were produced by the emission current in a few rf cycles. Most ions are created within a few microns of the emission center. Due to their large mass, the ions remain in the emitter vicinity for several rf cycles, and a high-density ion cloud builds up. The ion cloud performs three important functions: (1) It creates electric fields at the emission site far in excess of the applied field; (2) it neutralizes the emission current so that the space-charge limits mentioned above no longer apply; and (3) it bombards the rf surface to dissipate more power and release more gas. These effects combine to increase the emission current by several orders of magnitude. In turn, the rate of ion production is raised as well. The ionization process is therefore self-amplifying and leads to a runaway situation. The power dissipated by the emission current and the bombarding ions increases so dramatically that ultimately the macroemitter is destroyed (rf processing). Due to the elevated temperatures, additional large quantities of neutral gas are also released. They contribute further to the runaway situation. Only the finite energy stored in the cavity appears to limit the entire process. Even the melting of microemitters does not stop emission because the strong electric field created by the ions permits natural field emission. Based on the simulation, the positive feedback mechanism is so powerful that rf processing times should be considerably less than 1 μs. This time scale is consistent with experimental observations.

APPENDIX A   SIMULATION-SIZE CONSIDERATIONS

When considering the field-emission simulation problem, several different length scales need to be addressed:

1. *Emitter size*   Most microemitters appear to be about 0.5 μm or less in diameter. For accurate simulations, the mesh has to resolve this distance.
2. *Distance to the ionization region*   Emission electrons, when accelerated by the applied field, gain about 30 eV within distances shorter than 1 μm. At this point they are capable of ionizing most gases. To accurately simulate ionization, the mesh has to be finer than this distance.
3. *Size of the ionization region*   We need to ensure that most ionization occurs within the simulation region. Hence, the gas density should be low furthest from the emitter, or the electron energy there has to be too high for ionization (or both). At an applied field of 30 MV/m, this requirement is easily satisfied for distances greater or equal to 30 μm.
4. *Extent of the plasma cloud*   The ion cloud being created near the emitter expands with time. The size of the simulation region has to be large with respect to this cloud to minimize the impact of the (artificial) system boundaries on the field distribution. Due to computational limitations, our simulations can only cover a few rf periods. In this time, the cloud expands no more than a few microns.

A simulation region no less than a few 10 μm in size satisfies all four length scales. The requirement placed on the mesh density is quite stringent. Both items 1 and 2 demand mesh spacings of a fraction of a micron. On the order of 10^4 mesh elements are needed to cover the entire simulation region. Critical, also, is the fact that no charged particles are permitted to traverse more than one mesh

element in a time step for the field solver to function. Electron speeds of 10^7 m/s thus limit the time steps to about $dt = 10$ fs or less!

References

[1] H. Padamsee, J. Knobloch, and T. Hays, *RF Superconductivity for Accelerators*, Wiley and Sons, New York, 1998.

[2] R.H. Fowler and L. Nordheim, *Proceedings of the Royal Society London A* **119**, 173 (1928).

[3] R. Noer, *Applied Physics A* **28**, 1 (1982).

[4] J.H. Graber, High power processing studies of 3 GHz niobium superconducting accelerator cavities, PhD thesis, Cornell University, 1993, Laboratory of Nuclear Studies thesis CLNS 93-1.

[5] G.A. Mesyats, *IEEE Transactions on Electrical Insulation* **EI-18**, 218 (1983).

[6] E.A. Litvinov, G.A. Mesyats, and D.I. Proskurovskii, *Soviet Physics Uspekhi* **26**, 138 (1983).

[7] B. Jüttner, *Nuclear Instruments and Methods in Physics Research A* **268**, 390 (1988).

[8] J. Knobloch, Advanced thermometry studies of superconducting rf cavities, PhD thesis, Cornell University, 1997, Laboratory of Nuclear Studies thesis CLNS 97-3.

[9] J. Knobloch and H. Padamsee, *Particle Accelerators* **53**, 53 (1996), Also published in the Proceedings of the 7th Workshop on RF Superconductivity, Gif-sur-Yvette, France, pp. 95–103 (1995).

[10] J. Knobloch, H. Muller, and H. Padamsee, *Review of Scientific Instruments* **65**, 3521 (1994).

[11] H.A. Schwettman, J.P. Turneaure, and R.F. Waites, *Journal of Applied Physics* **45**, 914 (1974).

[12] D. Moffat *et al.*, *Particle Accelerators* **40**, 85 (1992).

[13] E.A. Litvinov, *IEEE Transactions on Electrical Insulation* **EI-20**, 683 (1985).

[14] G.K. Kartsev, G.A. Mesyats, D.I. Proskurovskii, V.P. Rotshtein, and G.N. Fursei, *Soviet Physics* **15**, 475 (1970).

[15] E. Hantzsche and B. Jüttner, *IEEE Transactions on Plasma Science* **PS-13**, 230 (1985).

[16] T. Hays *et al.*, Microscopic examination and elemental analysis of field emission sites in 5.8 GHz superconducting mushroom cavities, in *Proceedings of the 6th Workshop on RF Superconductivity*, edited by R. Sundelin, pp. 750–762, Newport News, VA, 1993.

[17] P. Kneisel, Surface preparation of niobium, in *Proceedings of the Workshop on RF Superconductivity*, edited by M. Kuntze, pp. 27–40, Karlsruhe, 1980, Proceedings also published as internal Kernforschungszentrum Kalsruhe report KFK-3019.

[18] T. Hays (Cornell University). Private communication.

[19] M. Pekeler, Untersuchungen der feldbegrenzenden Mechanismen in supraleitenden Niob-Resonatoren, PhD thesis, Deutsches Electronen-Synchrotron (DESY), 1996.

[20] N.S. Xu, The physical origin of prebreakdown electron "pin-holes", in *High Voltage Vacuum Insulation*, edited by R.V. Latham, pp. 115–164, Academic Press, London, 1995.

[21] P.A. Chatterton, *Proceedings of the Physical Society London* **88**, 231 (1966).

[22] Y.Y. Lau, Y. Liu, and R.K. Parker, *Physics of Plasmas* **1**, 2082 (1994).

[23] W. Weingarten, On electrical breakdown in superconducting accelerating cavities, in *Proceedings of the XIII International Symposium on Discharges and Electrical Insulation in Vacuum*, pp. 480–485, Paris, France, 1988.

[24] S. Bajic and R. Latham, *Journal of Physics D* **21**, 943 (1988).

[25] J. Halbritter, *IEEE Transactions on Electrical Insulation* **EI-18**, 253 (1983).

[26] G. Comsa and R. David, *Surface Science Reports* **5**, 145 (1985).

[27] Y. Okuno, K. Okuno, Y. Kaneko, and I. Kanomata, *Journal of the Physical Society Japan* **29**, 164 (1970).

[28] R.S. Freund, R.C. Wentzel, R.J. Shul, and T.R. Hayes, *Physical Review A* **41**, 3575 (1990).

[29] M.A. Lennon *et al.*, *Journal of Physical and Chemical Reference Data* **17**, 1285 (1988).

[30] H.C. Straub, B.G. Lindsay, K.A. Smith, and R.F. Stebbings, *Journal of Chemical Physics* **105**, 4015 (1996).

[31] D.P. Chernin, *IEEE Transactions on Electron Devices* **43**, 2004 (1996).

[32] D. Chernin, A. Drobot, and M. Kress, A model of secondary emission for use in computer simulation of vacuum electronic devices, in *Proceedings of the 1993 International Electron Devices Meeting*, pp. 773–776 (1993).

[33] J.D. Cobine, *Gaseous Conductors*, McGraw-Hill, New York, 1941.

[34] F.F. Chen, *Introduction to Plasma Physics*, Plenum Press, New York, 1974.

[35] T. Kubono, *Journal of Applied Physics* **49**, 3863 (1978).

[36] B. Jüttner, *IEEE Transactions on Plasma Science* **PS-15**, 474 (1987).

[37] G.M. Kassirov and G.A. Mesyates, *Soviet Physics – Technical Physics* **9**, 1141 (1965).

[38] A. Maitland, *Journal of Applied Physics* **32**, 2399 (1961).

[39] J. Halbritter, *IEEE Transactions on Electrical Insulation* **EI-20**, 671 (1985).

[40] G. Carter and J.S. Colligon, *Ion Bombardment of Solids*, American Elsevier Publishing, New York, 1968.

[41] N. Laegreid and G.K. Wehner, *Journal of Applied Physics* **32**, 365 (1961).

[42] D. Rosenberg and G.K. Wehner, *Journal of Applied Physics* **33**, 1842 (1962).

[43] S.K. Erents and G.M. McCracken, *Journal of Applied Physics* **44**, 3139 (1973).

[44] P. Niedermann, Experiments on enhanced field emission, PhD thesis, University of Geneva, 1986, Dissertation number 2197.

[45] A.I. Bushik, B. Jüttner, and H. Pursch, *Beiträge aus der Plasmaphysik* **19**, 177 (1979).

[46] G.N. Fursey, *IEEE Transactions on Electrical Insulation* **EI-20**, 659 (1985).